PAPER • OPEN ACCESS

Ultrafast quasi-three-dimensional imaging

View the article online for updates and enhancements.

Ultrafast quasi-three-dimensional imaging

Yiling Lian[1], Lan Jiang[1,2,3,*], Jingya Sun[1,2], Jiadong Zhou[4] and Yao Zhou[1,5]

[1] Laser Micro/Nano Fabrication Laboratory, School of Mechanical Engineering, Beijing Institute of Technology, Beijing 100081, People's Republic of China
[2] Yangtze Delta Region Academy of Beijing Institute of Technology, Jiaxing 314019, People's Republic of China
[3] Beijing Institute of Technology Chongqing Innovation Center, Chongqing 401120, People's Republic of China
[4] Centre for Quantum Physics, Key Laboratory of Advanced Optoelectronic Quantum Architecture and Measurement (MOE), School of Physics, Beijing Institute of Technology, Beijing 100081, People's Republic of China
[5] Advanced Research Institute of Multidisciplinary Sciences, Beijing Institute of Technology, Beijing 100081, People's Republic of China

E-mail: jianglan@bit.edu.cn

Abstract

Understanding laser induced ultrafast processes with complex three-dimensional (3D) geometries and extreme property evolution offers a unique opportunity to explore novel physical phenomena and to overcome the manufacturing limitations. Ultrafast imaging offers exceptional spatiotemporal resolution and thus has been considered an effective tool. However, in conventional single-view imaging techniques, 3D information is projected on a two-dimensional plane, which leads to significant information loss that is detrimental to understanding the full ultrafast process. Here, we propose a quasi-3D imaging method to describe the ultrafast process and further analyze spatial asymmetries of laser induced plasma. Orthogonally polarized laser pulses are adopted to illuminate reflection-transmission views, and binarization techniques are employed to extract contours, forming the corresponding two-dimensional matrix. By rotating and multiplying the two-dimensional contour matrices obtained from the dual views, a quasi-3D image can be reconstructed. This successfully reveals dual-phase transition mechanisms and elucidates the diffraction phenomena occurring outside the plasma. Furthermore, the quasi-3D image confirms the spatial asymmetries of the picosecond plasma, which is difficult to achieve with two-dimensional images. Our findings demonstrate that quasi-3D imaging not only offers a more comprehensive understanding of plasma dynamics than previous imaging methods, but also has wide potential in revealing various complex ultrafast phenomena in related fields including strong-field physics, fluid dynamics, and cutting-edge manufacturing.

Keywords: ultrafast imaging, extraction and reconstruction, quasi-three-dimension, plasma diffraction

---

* Author to whom any correspondence should be addressed.

1. Introduction

Although exploring laser-induced ultrafast processes is crucial in strong-field physics, fluid dynamics, and advanced manufacturing, ultrafast processes are difficult to understand in depth because the uneven spatial distribution of a laser field triggers a variety of non-equilibrium processes when interacting with materials, that result in different optical properties and a complex morphology of the excited region. The femtosecond pump-probe technique is widely recognized as an excellent tool for studying ultrafast dynamics [1, 2]. This technique enables the observation of rapid changes in electron density and temperature that occur following the interaction of an intense femtosecond laser pulse with a surface [3–6]. The resulting highly nonequilibrium state induces phase explosion [7, 8], Coulomb explosion [9, 10], and thermoelastic wave effects [11, 12], ultimately leading to the ablation and fracture of the target materials [13, 14]. To gain insight into the underlying ablation mechanisms, researchers have employed femtosecond pump-probe imaging to investigate transient optical properties [15, 16]. However, during the signal acquisition process, these ablation processes have a significant effect on the optical response of the target materials [17–19]. For example, when molybdenum disulfide (MoS_2) is ablated by a femtosecond laser [20], the rise in electron density leads to a reduction in reflectivity when probed by a 400 nm femtosecond laser pulse. The phase explosion maintains the molten state of MoS_2 at a low reflectivity level for an extended period. Therefore, it becomes challenging to distinguish the separate influences of these two factors on reflectance based solely on the acquired reflective images. In addition, in the case of gallium nitride [21] ablation at relatively low laser fluences, the transient reflectivity experiences a concomitant increase due to the Coulomb Explosion. Conversely, higher fluences result in the formation of an overheated liquid phase, that has pronounced absorption characteristics. In addition to the modification of optical signals arising from variations in material properties, the occurrence of Newton rings [22, 23] due to thin film interference phenomena introduces periodic patterns of bright and dark stripes. The superposition of these ablation characteristics and interference patterns makes it difficult to accurately determine the actual shape and properties of the ablation based solely based on the reflective image. Consequently, this presents challenges for the subsequent analysis of ablation characteristics.

In the specific context of side-view imaging of femtosecond laser ablation in aluminum [24], the distinctive processes involved in a material eruption can be identified through analysis of the observed shock wave profile. Two discernible phenomena should be noted. The first phenomenon is phase explosion triggered by high temperatures, resulting in the generation of a high-temperature plasma. The second phenomenon is due to the thermomechanical effects, in which the lattice rupture occurs under stress, ultimately leading to material eruption. However, these transformations are accompanied by a significant decrease in reflectivity [6], it is difficult to differentiate between them solely on the basis of reflective observations. From a side-view perspective, it is noteworthy that high laser

fluence induces the formation of an air breakdown channel prior to surface material eruption [25]. Consequently, this channel gives rise to a longitudinal bulge during subsequent eruptions [26]. However, due to the high transmission characteristics, the air breakdown channel lies outside the focal plane of reflective viewing, which brings challenges to direct observation. Researchers have investigated plasma properties from dual perspectives. While focusing on acquiring low fluence induced transient reflectivity images at the picosecond timescale [27], plasma eruptions during this temporal range are nearly imperceptible from the side-view perspective [25]. To observe plasma and shockwaves more effectively, a longer time delay in the nanosecond range becomes necessary, which allows for the progressive observation of transmission changes from the side-view perspective. This temporal discrepancy between the two perspectives presents a significant challenge in further comprehending the intricate dynamics of the laser ablation process. Therefore, conducting a comprehensive investigation of plasma properties from both perspectives is crucial to gain a more comprehensive understanding of the laser ablation process.

In this study, a methodology is proposed to overcome the inherent limitations of conventional ultrafast imaging techniques in studying ultrafast 3D processes. The presented approach revolutionizes the mutual interference of two perspective signals via orthogonally polarized probing pulses, enabling simultaneous observations of laser induced plasma dynamics from both the reflective and transmissive perspectives. Using the contrasting information provided by the two views, this study successfully discerns the Coulomb explosion and the phase explosion, and elucidates the complex diffraction phenomena occurring outside of the plasma system. In addition, a quasi-3D reconstruction method is introduced that involves contour extraction through binarization techniques followed by matrix rotation and multiplication. The resulting reconstructed images describe the optical characteristics at any desired location, allowing for a deeper understanding of plasma properties. Notably, the analysis of the reconstructed images unveils the presence of asymmetry in the contraction and divergence of the plasma in the actual 3D space, which is attributed to the subtle asymmetry induced by Gaussian pulses. In a meticulous analysis of the reconstructed images, the observation ability is improved from ultrafast 2D to quasi-3D, providing clarity and detail regarding the plasma properties. These findings substantially advance the current understanding of plasma dynamics and offer valuable insights into the complex dynamics involved, as well as facilitating future research and development in ultrafast imaging and related disciplines.

2. Experimental setup

The experimental setup and data processing method utilized in this study are depicted in figure 1. The single view imaging with probe pulse is shown at first. For the side view, the boundary between sample and air is in the middle of the field of view. During the ablation process, the transmittance changes
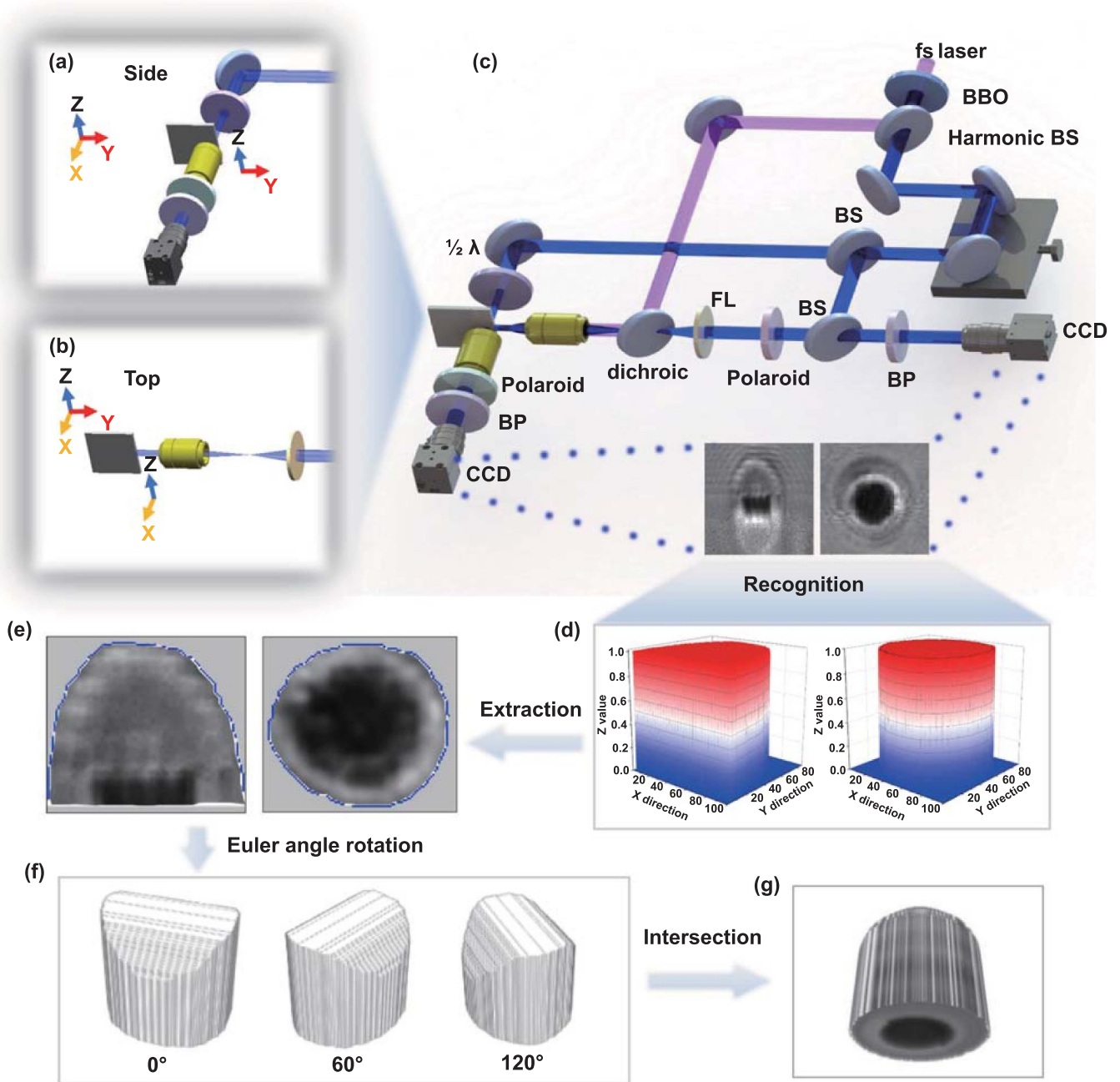
Figure 1. Experimental setup and operation scheme of the ultrafast quasi-3D imaging. BS: beam splitter, FL: focal lens, BP: bandpass filter, CCD: charge-coupled device. The (a) top and (b) side views are combined, as shown in (c), to catch the ablation and eruption dynamics of a sapphire during laser excitation with certain conditions. The demo is exhibited as indicated by dotted lines. The bottom part exhibits the image processing steps, including (d) recognition, (e) extraction, (f) rotation and (g) intersection.

when a material ejection occurs. For the top view, the prob- ing pulse enters the sample surface perpendicularly through the objective lens. During the ablation process, the material undergoes ultrafast phase changes, leading to instantaneous changes in the reflectivity. The side and top views are com- bined and the pump pulse is introduced, which enables the simultaneous detection of ultrafast processes from both per- spectives. Further details are provided below. The pulsed laser beams are generated using a Ti: sapphire chirped pulse amp- lification system (Spectra-Physics Spitfire Ace) operating at a wavelength of 800 nm and a pulse duration of 120 fs. To

facilitate the experimental procedure, an 800 nm beam split- ter is employed initially to split the pulses into two distinct beams: the pump pulse and the probe pulse. The pump pulse is responsible for exciting the target materials, whereas the probe pulse is utilized to investigate the dynamics and optical property changes resulting from the excitation. To control the delay time between the pump and probe pulses, a precise delay line is incorporated. The probe pulses are then frequency- doubled by passing through a beta barium borate crystal, res- ulting in the generation of 400 nm femtosecond laser pulses. These 400 nm pulses are subsequently split into two beams to

facilitate observation from both the top and side views. From the top view, the pump pulse is focused onto the target material through a specific objective (20×, NA 0.4, Olympus, Inc.), and the probe pulse is first focused onto the back focal plane of the same objective first and then propagated through the same objective. However, the side view observation utilizes a separate objective lens (50×, NA 0.5, Olympus, Inc.) to capture the shadowgraph. When the probing pulse arrives at the sample, scattering occurs in addition to besides reflection and transmission. The polished sample surface has nanoscale smoothness which can avoid scattering. Yet during laser irradiation, plasma eruption and structural formation enhance the scattering, leading to the photon scattering from the top to the side, in addition to signal anomalies. Photons from the side also enter the top in the same manner. Therefore, a half-wave plate (1/2 λ) and a polaroid are employed to manipulate the orthogonal polarization of the side and top view probe pulses, isolating the photon with different polarization and improving the signal-to-noise ratio of the images. To ensure precise synchronization, two delay stages with 10 fs time resolution are employed to adjust the two probe pulses to the same delay time. Furthermore, a long optical delay line is utilized to control the overall pump probe delay. Subsequently, the reflectivity and transmission shadowgraph of the plasma are imaged by a charge-coupled device (CCD) camera after passing through the polaroid and bandpass filters. The sample utilized in this experiment is a piece of sapphire with the dimensions of 10 × 10 × 1 mm, featuring three polished surfaces. The obtained reflection and transmission images are indicated by dashed lines and used for subsequent image processing. The bottom part of figure 1 illustrates the image processing procedure. First, the raw images undergo binarization to select the signal region. Then two contour matrices are established. By multiplying the contour matrices through rotation, a 3D matrix is formed.

3. Results and discussions

The reflectivity changes, as shown in figure 2(a), illustrate the irradiation process with a fluence of 90 J cm^{-2}. Initially, at a delay of 0.15 ps, the central region exhibits an increase in reflectivity, which manifests as a brighter appearance. Subsequently, as the delay is extended to 1.5 ps, the bright region expands, and distinctive bright and dark areas emerge at the periphery of the central region. This phenomenon stems from the variations in the energy distribution within the circular laser beam. In the center of the laser beam, the fluence is significantly higher compared to in the surrounding regions. Therefore, various processes, including multi-photon absorption and tunnel ionization, contribute to a rapid increase in the free electron density. As a result, the reflectivity undergoes a rapid increase in this central region. Conversely, the surrounding area of the laser beam experiences lower fluence, limiting the occurrence of tunnel ionization. Mechanisms such as multi-photon ionization and collision ionization become prominent when increasing the free electron density within

this region. Subsequently, the strong ionization induced by the laser triggers Coulomb explosion and ablation of the surface layer [28, 29] This leads to surface fluctuation and the formation of alternating diffraction rings. At a delay of 40 ps, the size of the central region remains unchanged, but its relative reflectivity decreases to a negative value. The decrease in reflectivity indicates the occurrence of melting and the formation of a liquid phase, which enhances light absorption.

At 600 ps compared to 40 ps, the melting process continues due to lattice thermal conduction, causing the central liquid area to expand. However, the liquid area remains at a high temperature, resulting in essentially unchanged reflectivity. The sustained high temperature prevents significant changes in the reflectivity of the liquid, even as the spatial extent of the liquid area expands. These observations highlight the dynamic evolution of the surface as it undergoes melting and liquid formation. The time-dependent changes in reflectivity provide valuable insights into the thermal and structural transformations that occur in the material under the influence of the intense laser pulse. Understanding these processes is crucial for the optimization of laser-material interactions and the development of laser-based applications.

At both 40 ps and 600 ps delays, alternating ring-shaped structures persist outside the central region. These structures result from the formation of a gasor gasliquid mixture during the expansion and compression of the air by the shock wave. The presence of the gas leads to diffraction of the probe pulse because the gas has a higher transmission rate and refractive index compared to air, causing alterations in the light field distribution. The subsequent material transition process primarily involves lattice thermal conduction, which continues the melting process. As the liquid cools during thermal conduction, its light absorption capability diminishes, making it transparent. This phenomenon can be observed in the central region at the 1200 ps delay. In figure 2(b), a two-dimensional sectional image is presented, illustrating the ultrafast reflective response with different excitation fluences. At 3 ps, the reflectivity change shifts from positive to negative for both fluences, indicating the onset of melting. This melting process represents the time required for the lattice to transition from an ordered state to oscillation until it becomes disordered. Among the observed materials, sapphire exhibits the fastest lattice disruption, occurring at approximately 3 ps. As the delay time increases, the material's reflectivity first continues to decrease from 3 ps to 10 ps, and it then starts to increase again around 1 ns as the molten liquid phase cools. When subjected to 90 J cm^{-2} irradiation, the reflectivity rises more rapidly and reaches higher extremes before the subsequent increase. However, the radius of the signal region remains consistent at 1.5 μm for both irradiation fluences. Further radial expansion of the melt region only occurs 30 ps later when radial heat conduction takes place.

The extracted central reflectivity in figure 2(c) is divided into three distinct stages. In Stage 1, the high fluence leads to a rapid increase in the relative reflectivity above zero, indicating the occurrence of Coulomb explosion. Stage 2 is characterized by a decrease in relative reflectivity below zero,
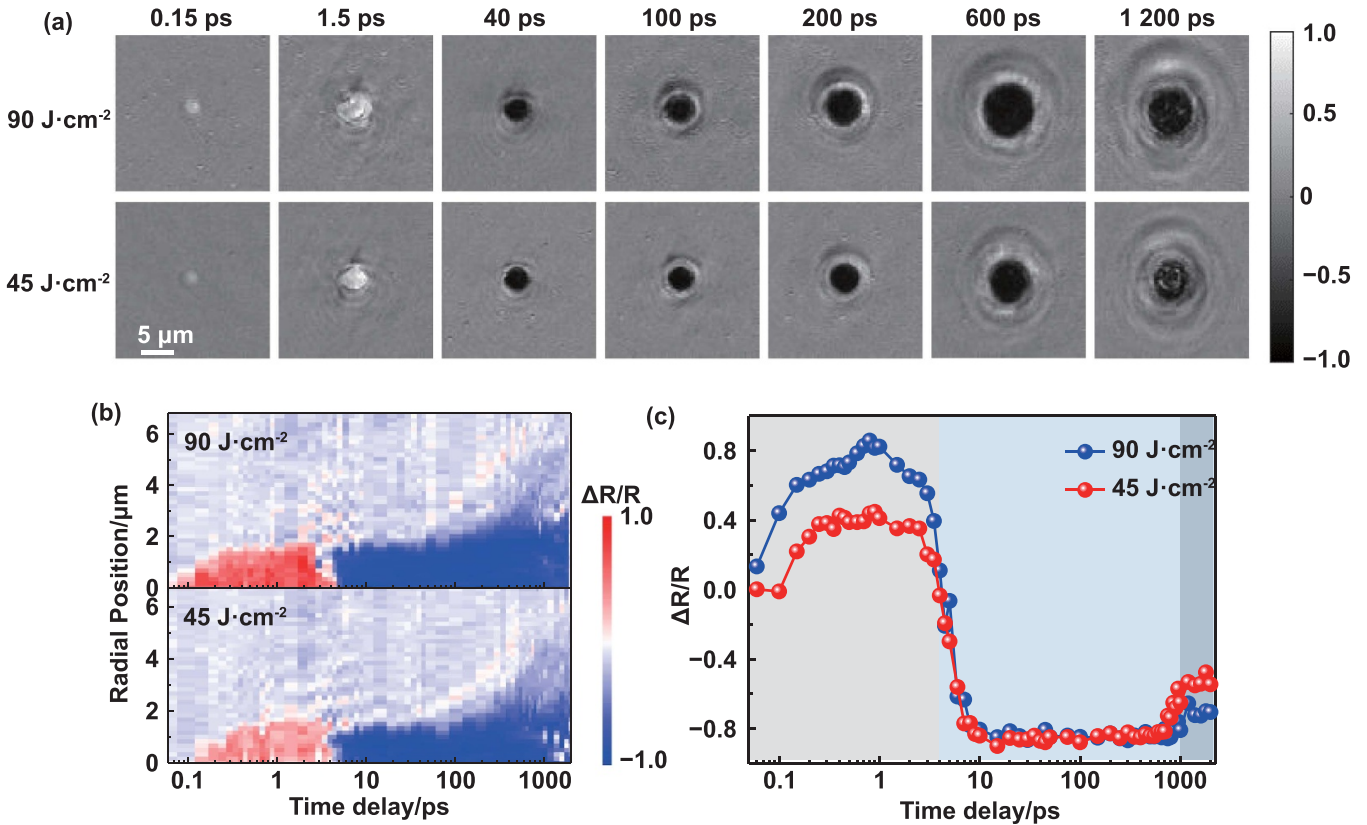
Figure 2. Ultrafast reflectivity dynamics after laser excitation with various fluences. (a) 2D mapping of the transient reflectivity at delay times from 0.15 ps to 1200 ps with irradiation with fluences of 45 J cm^{-2} and 90 J cm^{-2}. (b) Spatial reflectivity distribution extracted from the diameter axis of the focal area of 45 J cm^{-2} and 90 J cm^{-2}. (c) Time-resolved central reflectivity extracted from the 2D mappings.

signifying a phase explosion induced by high temperature. During this stage, the melting phase exhibits strong light absorption capability. In Stage 3, the melting phase begins to cool, resulting in an increase in reflectivity of approximately 1 ns. The maximum reflectivity values differ between the two induced cases, at approximately 0.4 for the 45 J cm^{-2} case and 0.8 for the 90 J cm^{-2} case. Figure 2 provides valuable insights into the material's phase transition process based on the reflectivity evolution. However, it is important to note that the observed phenomena primarily represent projections near the focal plane of the reflectance view. This limitation restricts the comprehensive description of the plasma properties.

To enhance understanding of plasma dynamics and provide a more comprehensive view of the ablation process, the simultaneous side-view images of the ablation process are captured, as shown in figure 3. Figure 3 presents images from a side perspective, offering valuable insight into the dynamics of plasma evolution and enabling a deeper understanding of plasma generation, expansion, and cooling. In both the 45 J cm^{-2} and 90 J cm^{-2} cases, distinct features are observed at the air-sample interface at 5 ps, with the presence of a black region and a bright region. At 2 ps, only air disruption is observed. By excluding the influences of diffraction, interference, and other phenomena, and considering the conclusions drawn from figure 2, it can be inferred that the bright region corresponds to a low-density plasma formed by Coulomb

explosion, which is distinct from the melting liquid phase and air plasma. Conversely, the dark region represents the formation of a liquid induced by phase explosion, as indicated in figure 2. As the delay time increases, both the bright and dark regions expand outward. As shown in figure 3(b), the transmittance of the bright region gradually decreases and reaches the same level as the background region. Further, increasing the delay to 300 ps results in a more pronounced boundary between the bright and dark regions, forming a distinct two-layer ejection contour.

It is noteworthy that the aspect ratios of the two-layer contour differ, with their longitudinal expansion rates being similar. However, the radial expansion rate of the outer layer contour is significantly higher compared to that of the inner layer contour. This discrepancy arises due to the expansion of the outer plasma under with the influence of air breakdown. As the plasma expands, it compresses the surrounding air, creating a low-pressure area that reduces resistance. This reduced resistance facilitates the subsequent ejection of the liquid phase. The internal morphology of with liquid exhibits similarities to plasma ejections in near-vacuum atmospheres. Thus, the radial expansion distance approximately matches the measured dynamic melting diameter at the interface [29–33]. These observations further contribute to understanding of plasma dynamics and the associated physical phenomena.
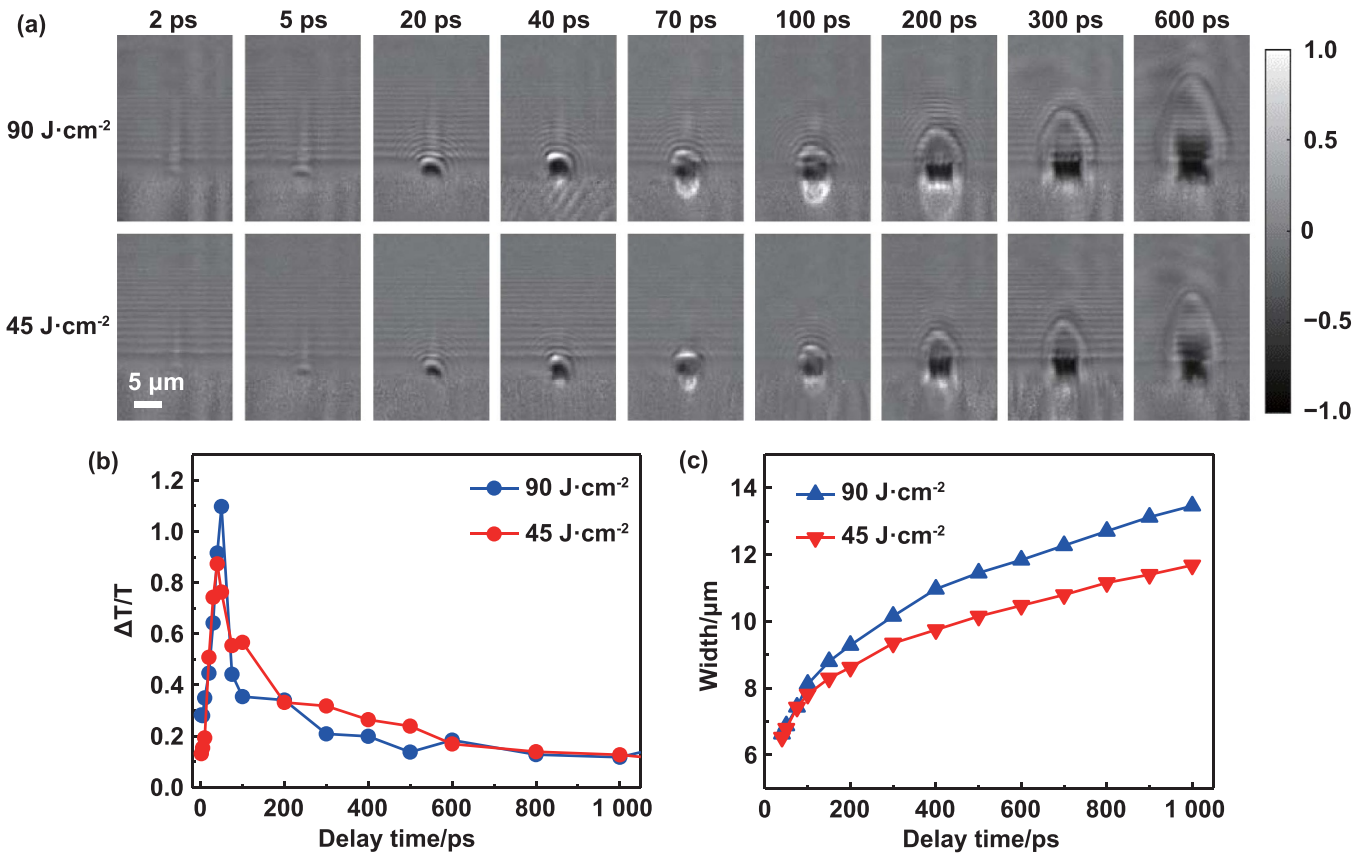
Figure 3. Ultrafast transmission dynamics after laser excitation with various fluences. (a) Transient relative transmissivity evolution $\Delta T/T$ of sapphire excited with 45 J cm^{-2} and 90 J cm^{-2}. (b) The relative transmittance of the front edge of the ablation plume. (c) The width of the shockwave at the ablation boundary.

To overcome certain limitations in the individual images and enhance the interpretation of the experimental results, clarifying annotations and alignment are introduced in figure 4. These improvements aid in visualizing the characteristic parameters and provide a more accurate representation of the shockwave boundary and the nature of the alternating rings observed in the reflective image. Specifically, in figure 4(a), yellow arrows are used as annotations to mark the key boundary at the interface. One side of the boundary represents the width of the liquid phase, and the other side represents the width of the shockwave edge. This annotation scheme offers a clearer visualization of the characteristic parameters, which allows for a better comparison of the two perspectives. Furthermore, the dotted line in figure 4(b) corresponds to the characteristic images from two perspective views. This alignment enhances the accuracy of the comparison between the reflective and transmission images, facilitating a more precise interpretation of the experimental results. By providing an accurate representation of the shockwave boundary and clarifying that the alternating rings observed in the reflective image are surface diffraction rings, figure 4 addresses a long-standing misunderstanding that these rings may be related to Newton's rings. This correction ensures a more reliable understanding of the phenomenon and ensures an accurate interpretation of the experimental findings. Overall, the improvements introduced in figure 4 contribute to a more comprehensive and accurate

analysis of the plasma dynamics, overcoming previous limitations and providing valuable insights into the experimental results.

Different from that true 3D images originate from experimental measurements. The quasi-3D image is based on integrated projections of a real object from two orthogonal views. By rotating and multiplying the matrices corresponding to the two views, the reconstructed image exhibits 3D characteristics. However, the reconstructed image does not have the exact details as real objects, it is referred to as quasi-3D. The construction algorithms involve several important factors and implementation steps to ensure accurate and comprehensive results [34, 35]. The first step is image processing which involves preprocessing top view and side view images to enhance their clarity and remove any noise or artifacts. This ensures that the images are ready for further analysis and fusion. The next step is matrix transformation, in which the 2D images are transformed into matrices that represent the intensity values of each pixel. These matrices serve as the basis for subsequent calculations and manipulations.

Matrix multiplication is then performed to combine the information from the top view and side view matrices. This multiplication process allows for the extraction of 3D coordinate points that represent the spatial distribution of the plasma. To account for the different viewing perspectives, rotation
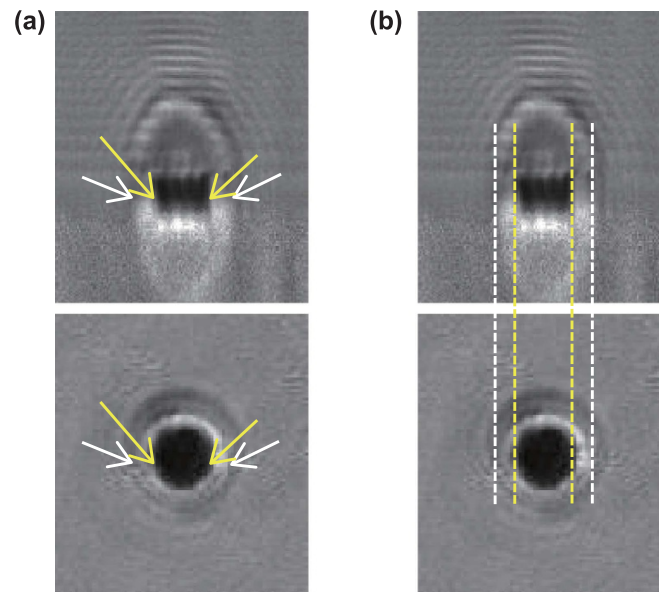
Figure 4. Feature position marking and alignment of two perspective images. (a) The arrows mark key boundaris in the two perspective images. (b) The dashed lines correspond to characteristic regions in two perspective images. The image obtained at a 200 ps delay for 90 J cm^{-2} irradiation is chosed as the example in (a) and (b).

matrices are constructed based on the geometric relationship between the two views. These rotation matrices enable the transformation of the 3D coordinate points to align with the desired viewing perspective. The rotated 3D image is then formed by applying the image rotation function to the 3D coordinate points. This process ensures that the reconstructed image accurately represents the spatial distribution of the plasma from multiple perspectives. Finally, the rotated images from multiple perspectives are synthesized into a single image by taking the intersection of the pixel values. This merging process creates a comprehensive quasi-3D image that combines the information from both the top view and side view, providing a more complete understanding of the plasma dynamics.

These steps and algorithms are applied to the images obtained at 200 ps delay under 90 J cm^{-2} irradiation, allowing for the reconstruction of a quasi-3D image that accurately represents the properties and distribution of the plasma at specific time point. By employing these extraction-reconstruction algorithms, we can overcome the limitations of individual views and obtain a more comprehensive understanding of plasma dynamics in three dimensions [36–40]. This approach enhances our ability to analyze and interpret the experimental results, leading to valuable insights and advancements in the field.

(I) The grayscale images of the top and side views are imported and subsequently binarized by applying a threshold. The resulting binarized matrices, Matrix-Top and Matrix-Side, are obtained by inverting the colors, as shown in figures 5(a) and (b). In the figures, zero represents the background and one represents the signal region in the images. The corresponding

original images and recognized contours are shown in figures 5(c) and (d).

(II) The dimensions of Matrix-Top and Matrix-Side are determined by calculating the number of rows and columns for each matrix. The maximum values of Row-Length-Top, Column-Length-Top, Row-Length-Side, and Column-Length-Side are then taken to obtain the final dimensions, Row-Length and Column-Length.

(III) To ensure equal dimensions between Matrix-Top and Matrix-Side, an all-ones matrix of size Row-Length × Column-Length, named One-Total-Length-Matrix, is constructed. Additional all-ones matrices are vertically appended to Matrix-Side, aligning it with Matrix-Top.

(IV) By defining a as zero and b as one, the inverse matrices of zero and one are obtained by replacing their respective values in MatrixSidever2 and MatrixTopver2. This allows for the creation of the rotation matrix, ThreeDimensionDataVer1. The three-dimensional coordinate points are then obtained by multiplying each row in MatrixTopver2 with each column in MatrixSidever2.

(V) A set of 36 rotation matrices, spanning a range of 360°, are constructed as shown in figure 6(a). The 3D images are rotated using these matrices to form a list, Image3DLists, containing the rotated 3D images [41]. The different perspectives of the 3D graphics are intersected to generate a single image representing three complete 3D graphics. Notably, during the rotation process, the gray value of the transmission viewing perspective is assigned to the reconstructed 3D matrix. The reconstructed contour images and quasi-3D plasma images are exhibited in figure 6(b) with three views.
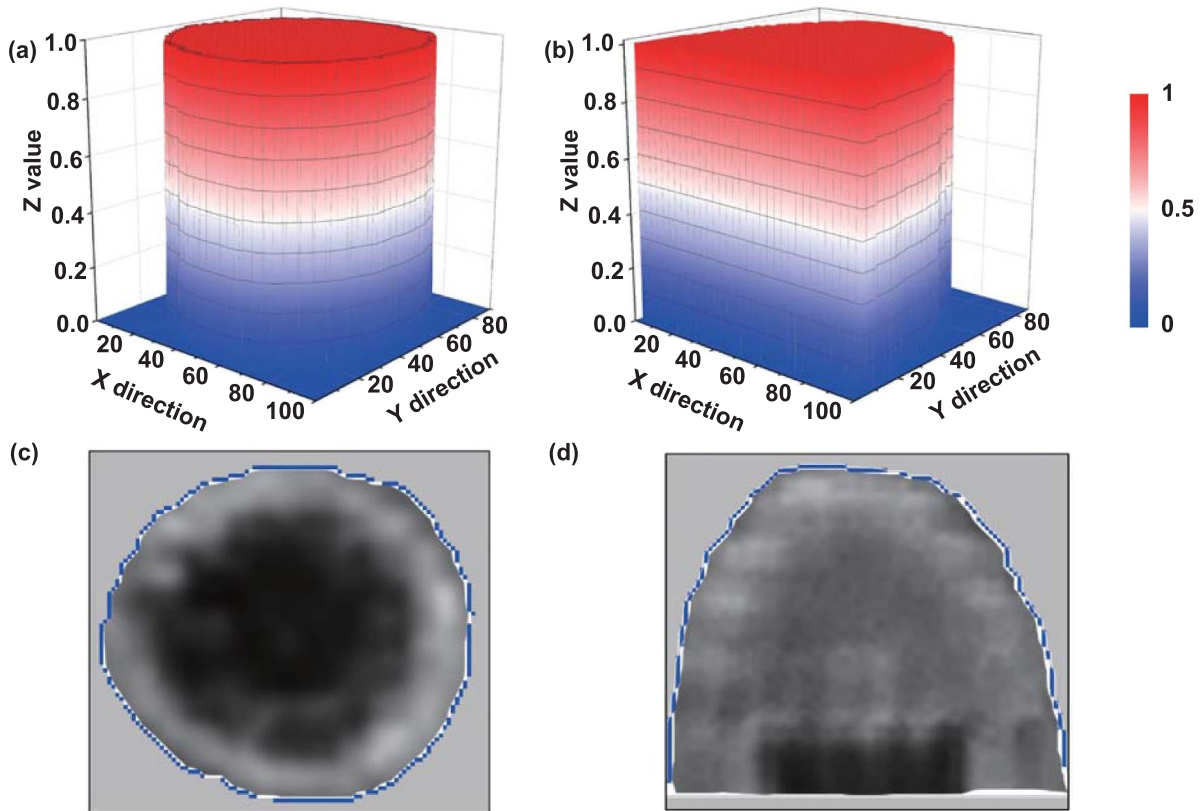
Figure 5. The boundary segmentation images. The boundary segmentation images obtained from binarization in the (a) reflection and (b) transmission perspectives, (c) and (d) are the recognized images corresponding to (a) and (b), and the blue dot represents the recognized contour.

The reconstructed quasi-3D images and the section images at the delay times of 100 ps and 200 ps are shown in figure 7. Through this type of such reconstruction, the contours and optical properties of any cross-section can be extracted at any section of the quasi-3D images, leading to a clearer understanding of the plasma dynamics in 3D space.

When relying solely on the reflective perspective, the central region is typically presumed to represent surface reflectivity. However, the true condition can only be unveiled by combining it with the other image perspectives, and describing the three-dimensional dynamics purely through two-dimensional images can be challenging. Nevertheless, the reconstructed quasi 3D image in figure 7(a) provides a direct and systematic understanding of the optical properties. In this image, yellow denotes low transmittance, while white represents high transmittance. By examining this quasi-3D representation, a more comprehensive comprehension of the optical properties can be achieved. The two distinct contours described in figure 3 can be directly distinguished. When light propagates within the plasma, the outer contour exhibits high transmittance, while the inner contour displays low transmittance. Taking the inner contour as an example, the transmittance gradually decreases from the eruptive front to the surface. As the light reaches the surface, it is mostly absorbed, resulting in a relative reflectivity at the center below -0.9 (see figure 2). However, the high transmittance observed in the outer contour indicates the probing light transmitted to the surface annular region is greater than the average light intensity of the background region. This leads to an increase in the relative reflectivity after the completion of the 200 ps electron relaxation, forming a bright ring. This capability allows the complex three-dimensional characteristics of the plasma to be assessed based on a single image.

In previous studies, the eruption rate and pressure has been measured when analyzing the transmissive perspective. The introduction of quasi 3D reconstruction makes it impossible to analyze the transmissive cross-sections at any desired location. As illustrated in figures 7(b) and (c), the transmissive cross-sections at 1/3 and 2/3 of the radius, respectively, are extracted from the *X* and *Y* axes at a delay of 200 ps. This advancement enables a more comprehensive analysis of the laser ablation process from different cross-sectional perspectives, providing valuable insights into the dynamic behavior of the plasma. Overall, the properties of the cross-sections in both directions are generally similar. When approaching the center ($R = 1/3$), the bottom of the cross-section exhibits a molten liquid phase, representing a low transmittance rate, whereas the top contour of the cross-section is
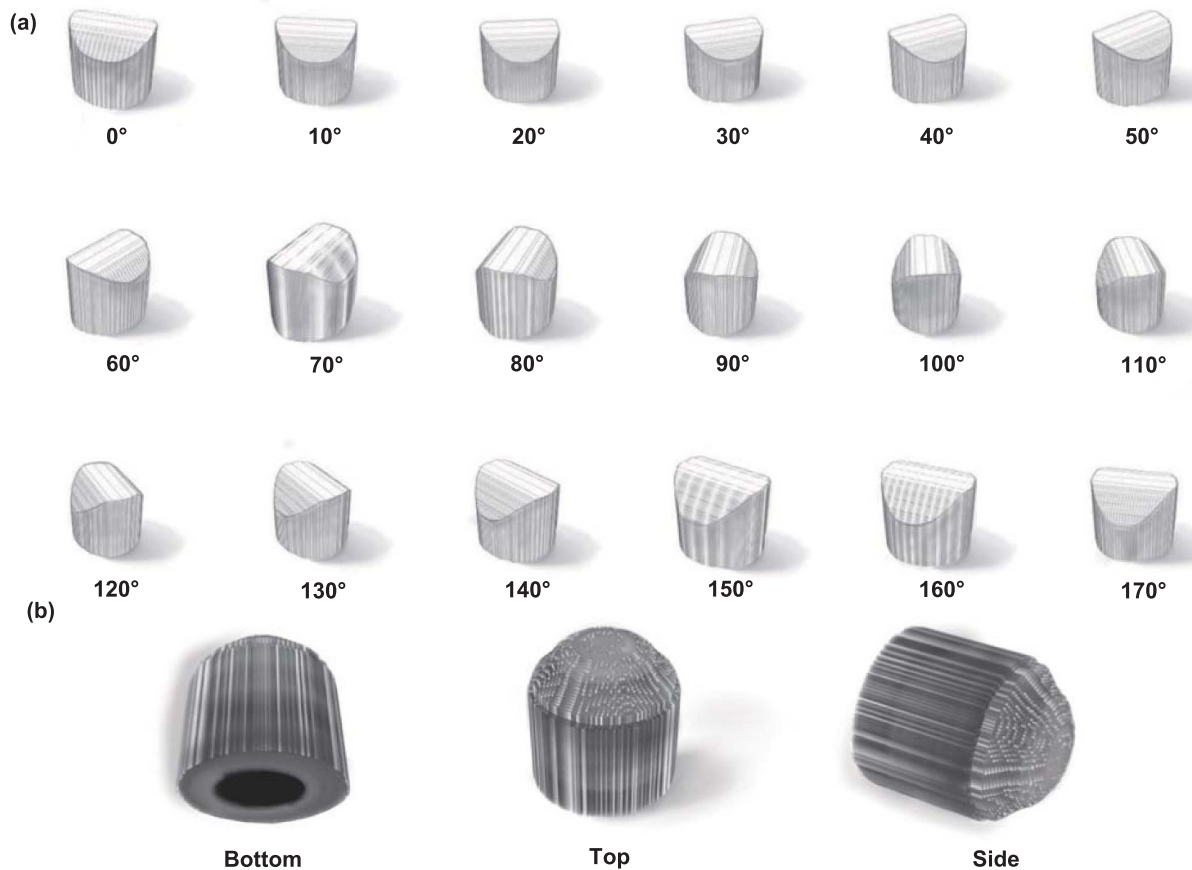
Figure 6. The reconstruction process and reconstructed images. (a) The process involves the matching and reconstructing of the 3D contour images from 18 different angles. (b) Views of the 3D plot from the bottom, top and side.

relatively smooth. When moving towards the edge ($R = 2/3$), the entire cross-section is located within the outer contour, and a decreasing transmittance rate from top to bottom can be observed, with a sharper top contour. Importantly, based on the cross-sectional images from different positions, the early asymmetrical eruption of the plasma can be detected. As shown in figure 7(b), at the $-1/3$ R and $1/3$ R positions along the same axis, the opaque region representing the phase explosion is asymmetric, with a converging front at $-1/3$ R and a diverging front at $1/3$ R. Furthermore, in figures 7(b) and (c), at the same cross-sectional position, the contraction and divergence of the opaque region are also different. To better demonstrate the advantages of quasi-3D imaging over 2D imaging, partial cross-sectional images from figures 7(b) and (c) are compared with the corresponding cross-sectional image at 100 ps in figure 7(d). It can be observed that for the central cross-section at different delays, the size of the plasma morphology in the dark region remains consistent, with differences only in contraction (X-axis) and divergence (Y-axis). At the $1/3$ R cross-section along the Y-axis, significant differences are observed at different delays. At 200 ps, the plasma exhibits symmetry between the left and right ends, whereas

at the earlier delay of 100 ps, the intensity of the plasma ejection is much lower on the left side than on the right side. It can be inferred that the spatial asymmetry of the plasma is stronger at 100 ps. Plasma ejection becomes more uniform after 200 ps, and then transforms into an asymmetrical shape again during subsequent structural formation processes (see figures 2, 1200 ps). The explanation can be provided as follows: The inability of the Gaussian beam profile to achieve perfect circularity leads to variations in the ionization intensity across different regions during the induction of air ionization. Specifically, when the transmittance perspective aligns with the axis of symmetry of the imaging plane, while the other positions remain asymmetric, early onset of plasma asymmetry is observed in this particularly region. This is difficult to discern from the individual perspectives of two-dimensional imaging in figures 2 and 3. Exploring information from other planes using 2D imaging can lead to blurriness and greater information loss due to defocusing. However, quasi-3D imaging is not constrained by these limitations, and fully utilizes the information of each point in 3D space. This contributes significantly to the advancement of comprehension regarding the 3D characteristics of plasma.
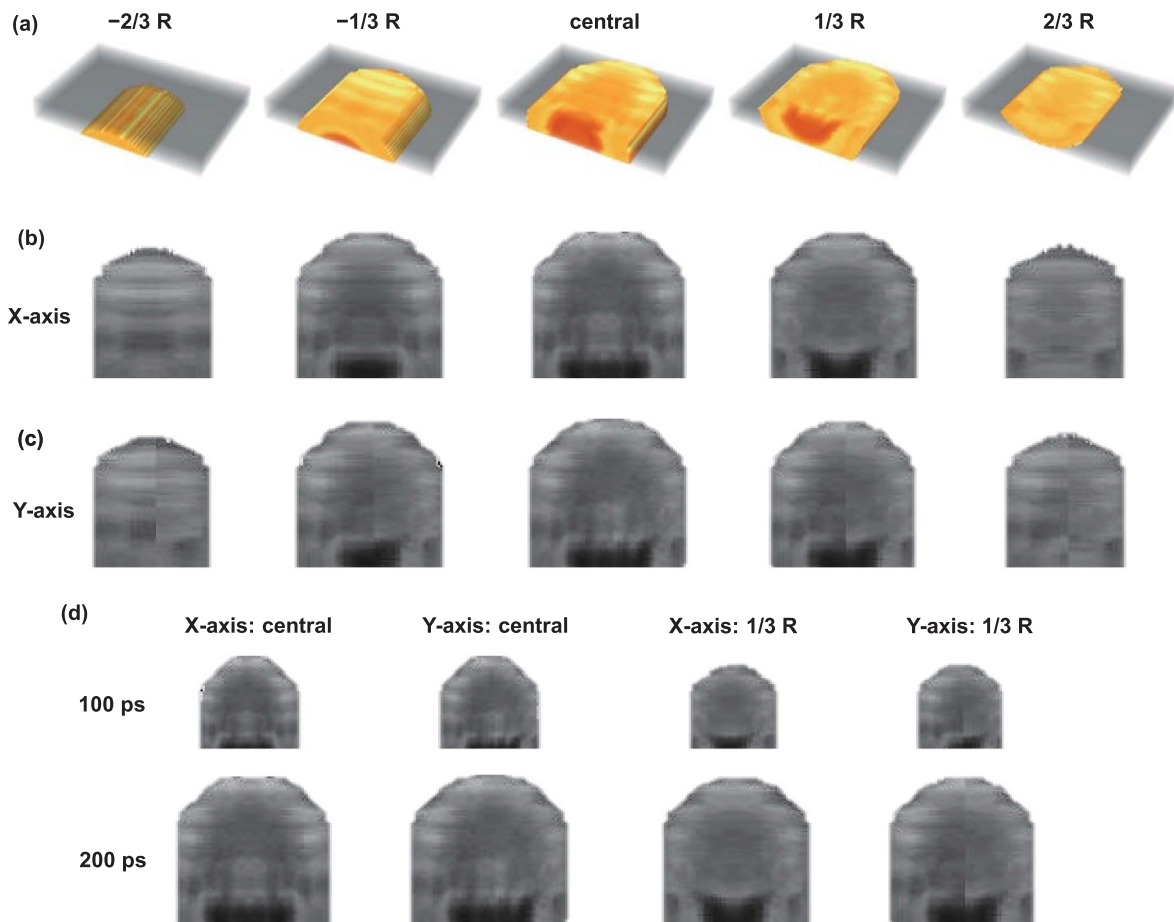
Figure 7. The cross-section images extracted from the reconstructed image. (a) The cross-sectional view images extract from the direction perpendicular to the *X*-axis. The cross-section images are exhibited as 3D shapes. Yellow represents low transmittance and white represents high transmittance. A cross-sectional view from the direction perpendicular to the (b) *X*-axis and (c) *Y*-axis. The cross-section images are exhibited as 2D images. Black represents low transmittance and white represents high transmittance. (d) Comparison of partial cross-sectional images with delays of 100 ps and 200 ps.

4. Conclusion

This study presents a novel quasi-3D imaging technique that overcomes the limitations of traditional imaging methods, enabling a more comprehensive analysis of the ultrafast process. By utilizing orthogonal polarization probe laser pulses, signal interference during the dual-perspective imaging of sapphire plasma is successfully eliminated, yielding high-quality reflectance-transmittance images. Through a meticulous comparison of the two perspectives, Coulomb explosion and phase explosion mechanisms were confirmed, and diffraction phenomena outside the plasma are discerned. A binary contour extraction and matrix rotation multiplication method is proposed to reconstruct a quasi-3D image, allowing the analysis of optical properties along any desired cross-section of the ultrafast process. The reconstructed plasma image reveals the presence of asymmetry in the contraction and expansion morphology of the plasma in 3D space. The quasi-3D imaging method not only augments our understanding of material ablation mechanisms, but also enhances the analytical dimension of ultrafast processes, which has widespread potential in many ultrafast fields.

Acknowledgments

ORCID iDs

Yiling Lian https://orcid.org/0009-0003-2197-1826
Lan Jiang https://orcid.org/0000-0003-0488-1987
Jingya Sun https://orcid.org/0000-0003-1884-6592

References

[1] Guo B S, Sun J Y, Lu Y F and Jiang L 2019 Ultrafast dynamics observation during femtosecond laser-material interaction *Int. J. Extreme Manuf.* **1** 032004
[2] Jiang L, Wang A D, Li B, Cui T H and Lu Y F 2018 Electrons dynamics control by shaping femtosecond laser pulses in micro/nanofabrication: modeling, method, measurement and application *Light Sci. Appl.* **7** 17134

[3] Winkler T, Haahr-Lillevang L, Sarpe C, Zielinski B, Götte N, Senftleben A, Balling P and Baumert T 2018 Laser amplification in excited dielectrics *Nat. Phys.* **14** 74–79

[4] Ning Z Q, Lian Y L, Jiang L, Sun J Y, Wu S Y and Wang F F 2022 Femtosecond laser-induced anisotropic structure and nonlinear optical response of yttria-stabilized zirconia single crystals with different planes *ACS Appl. Mater. Interfaces* **14** 39591–600

[5] Yao J L, Qi D L, Liang H T, He Y L, Yao Y H, Jia T Q, Yang Y, Sun Z R and Zhang S A 2022 Exploring femtosecond laser ablation by snapshot ultrafast imaging and molecular dynamics simulation *Ultrafast Sci.* **2022** 9754131

[6] Winter J, Rapp S, Spellauge M, Eulenkamp C, Schmidt M and Huber H P 2020 Ultrafast pump-probe ellipsometry and microscopy reveal the surface dynamics of femtosecond laser ablation of aluminium and stainless steel *Appl. Surf. Sci.* **511** 145514

[7] Perez D and Lewis L J 2002 Ablation of solids under femtosecond laser pulses *Phys. Rev. Lett.* **89** 255504

[8] Perez D and Lewis L J 2003 Molecular-dynamics study of ablation of solids under femtosecond laser pulses *Phys. Rev.* B **67** 184102

[9] Gamaly E G, Rode A V, Luther-Davies B and Tikhonchuk V T 2002 Ablation of solids by femtosecond lasers: ablation mechanism and ablation thresholds for metals and dielectrics *Phys. Plasmas* **9** 949–57

[10] Rethfeld B 2004 Unified model for the free-electron avalanche in laser-irradiated dielectrics *Phys. Rev. Lett.* **92** 187401

[11] Trovatello C *et al* 2020 Strongly coupled coherent phonons in single-layer MoS_2 *ACS Nano* **14** 5700–10

[12] Lian Y L *et al* 2021 Martensitic transformation in temporally shaped femtosecond laser shock peening 304 steel *Appl. Surf. Sci.* **567** 150855

[13] Balage P, Lopez J, Bonamis G, Hönninger C and Manek-Hönninger I 2023 Crack-free high-aspect ratio holes in glasses by top–down percussion drilling with infrared femtosecond laser GHz-bursts *Int. J. Extrem. Manuf.* **5** 015002

[14] Wang A D, Sopeña P and Grojo D 2022 Burst mode enabled ultrafast laser inscription inside gallium arsenide *Int. J. Extrem. Manuf.* **4** 045001

[15] Liu J K, Qin Z Y, Lu M, Ju J Q, Cao K Q, Chen L, Cheng K and Huo Y Y 2022 Ultrafast imaging analysis of femtosecond laser induced periodic nanoripples on Al film *Appl. Phys.* B **128** 88

[16] Liang J Y and Wang L V 2018 Single-shot ultrafast optical imaging *Optica* **5** 1113–27

[17] Wang D, Wei S B, Yuan X D, Liu Z Y, Weng Y Y, Zhou Y Q, Xiao T H, Goda K, Liu S and Lei C 2022 Ultrafast imaging for uncovering laser–material interaction dynamics *Int. J. Mech. Syst. Dyn.* **2** 65–81

[18] Sun Z L, Chen J H and Rudolph W 2011 Determination of the transient electron temperature in a femtosecond-laser-induced air plasma filament *Phys. Rev.* E **83** 046408

[19] Domke M, Rapp S, Schmidt M and Huber H P 2012 Ultrafast pump-probe microscopy with high temporal dynamic range *Opt. Express* **20** 10330–8

[20] Pan C J, Jiang L, Sun J Y, Wang Q S, Wang F F, Wang K, Lu Y F, Wang Y L, Qu L T and Cui T H 2020 Ultrafast optical response and ablation mechanisms of molybdenum disulfide under intense femtosecond laser irradiation *Light Sci. Appl.* **9** 80

[21] Wang F F, Jiang L, Sun J Y, Pan C J, Lian Y L, Sun J X, Wang K, Wang Q S, Wang J X and Lu Y F 2021 One-step fabrication method of GaN films for internal quantum efficiency enhancement and their ultrafast mechanism investigation *ACS Appl. Mater. Interfaces* **13** 7688–97

[22] Satoh D, Shibuya T, Terasawa E, Moriai Y, Ogawa H, Tanaka M, Kobayashi Y and Kuroda R 2020 Ultrafast pump-probe microscopic imaging of femtosecond laser-induced melting and ablation in single-crystalline silicon carbide *Appl. Phys.* A **126** 795

[23] Rapp S, Rosenberger J, Domke M, Heise G, Huber H P and Schmidt M 2014 Ultrafast pump-probe microscopy reveals the mechanism of selective fs laser structuring of transparent thin films for maskless micropatterning *Appl. Surf. Sci.* **290** 368–72

[24] Zhang N, Zhu X N, Yang J J, Wang X L and Wang M W 2007 Time-resolved shadowgraphs of material ejection in intense femtosecond laser ablation of aluminum *Phys. Rev. Lett.* **99** 167602

[25] Wang Q S, Jiang L, Sun J Y, Pan C J, Han W N, Wang G Y, Wang F F, Zhang K H, Li M and Lu Y F 2018 Structure-mediated excitation of air plasma and silicon plasma expansion in femtosecond laser pulses ablation *Research* **2018** 5709748

[26] Wang Q S, Jiang L, Sun J Y, Pan C J, Han W N, Wang G Y, Zhang H, Grigoropoulos C P and Lu Y F 2017 Enhancing the expansion of a plasma shockwave by crater-induced laser refocusing in femtosecond laser ablation of fused silica *Photon. Res.* **5** 488–93

[27] McDonald J P, Nees J A and Yalisove S M 2007 Pump-probe imaging of femtosecond pulsed laser ablation of silicon with thermally grown oxide films *J. Appl. Phys.* **102** 063109

[28] Wang M L, Mei W and Wang Y 2019 Simulation of femtosecond laser ablation sapphire based on free electron density *Opt. Laser Technol.* **113** 123–8

[29] Varel H, Wähmer M, Rosenfeld A, Ashkenasi D and Campbell E E B 1998 Femtosecond laser ablation of sapphire: time-of-flight analysis of ablation plume *Appl. Surf. Sci.* **127–129** 128–33

[30] Mora P 2003 Plasma expansion into a vacuum *Phys. Rev. Lett.* **90** 185002

[31] Nefedtsev E V and Batrakov A V 2015 Numerical simulations of stable explosive-emission center plasma expansion in vacuum *J. Exp. Theor. Phys.* **121** 706–16

[32] Freeman J R, Harilal S S, Diwakar P K, Verhoff B and Hassanein A 2013 Comparison of optical emission from nanosecond and femtosecond laser produced plasma in atmosphere and vacuum conditions *Spectrochim. Acta* B **87** 43–50

[33] Kuwahara A, Murakami K, Tomita H, Sawada K and Enokida Y 2022 Doppler splitting and expansion dynamics of laser-produced plasma plume under a high vacuum ambience *J. Anal. At. Spectrom.* **37** 2033–41

[34] Osorio Quero C, Durini D, Rangel-Magdaleno J, Martinez-Carranza J and Ramos-Garcia R 2022 Single-pixel near-infrared 3D image reconstruction in outdoor conditions *Micromachines* **13** 795

[35] Ma Z L and Liu S L 2018 A review of 3D reconstruction techniques in civil engineering and their applications *Adv. Eng. Inf.* **37** 163–74

[36] Li M Y, Du Z J, Ma X X, Dong W and Gao Y Z 2021 A robot hand-eye calibration method of line laser sensor based on 3D reconstruction *Robot. Comput.-Integr. Manuf.* **71** 102136

[37] Shrestha P, Xie C, Shishido H, Yoshii Y and Kitahara I 2022 3D reconstruction of bone from multi-view x-ray images using planar markers *Proc. 2022 IEEE 4th Global Conf. on Life Sciences and Technologies (Lifetech)* (IEEE) pp 189–93

[38] Uygur S Ö, Aydin C and Akyilmaz O 2022 Retrieval of Euler rotation angles from 3D similarity transformation based on quaternions *J. Spat. Sci.* **67** 255–72

[39] Yang M and Cho S I 2021 High-resolution 3D crop reconstruction and automatic analysis of phenotyping index using machine learning *Agriculture* **11** 1010

[40] Wang A, Das A, Hermann J and Grojo D 2021 Three-dimensional luminescence microscopy for quantitative plasma characterization in bulk semiconductors *Appl. Phys. Lett.* **119** 041108

[41] Milligan T 1999 More applications of Euler rotation angles *IEEE Antennas Propag. Mag.* **41** 78–83